Applications of Uncrewed Aerial Vehicles (UAVs) in Winter Precipitation-Type Forecasts

DANIEL D. TRIPP,[a] ELINOR R. MARTIN,[a] AND HEATHER D. REEVES[b,c]

[a] School of Meteorology, University of Oklahoma, Norman, Oklahoma
[b] Cooperative Institute for Mesoscale Meteorological Studies, University of Oklahoma, Norman, Oklahoma
[c] NOAA/OAR/National Severe Storms Laboratory, Norman, Oklahoma

ABSTRACT: Temperature and humidity profiles in the lowest 3 km of the atmosphere provide crucial information in determining the precipitation type, which aids forecasters in relaying winter-weather risks. In response to the challenges associated with forecasting mixed-phase environments, this study employs uncrewed aerial vehicles (UAVs) to explore the efficacy of high-resolution temporal and vertical measurements in winter-weather environments. On 19 February 2019, boundary layer measurements of an Oklahoma winter storm were collected by a UAV and radiosondes. UAV observations show a pronounced surface-based subfreezing layer that corresponds to observed ice pellets at the surface. This is in contrast to the High-Resolution Rapid Refresh (HRRR) model analyses, which show a subfreezing layer near the surface that is 3°C warmer than both the UAV and radiosonde observations. Using a spectral-bin-microphysics algorithm designed to provide hydrometeor-phase diagnosis throughout the vertical column, it was found that UAV measurements can improve discrimination between hydrometer types in environments near 0°C. A numerical-modeling study of the same winter-weather event illustrates the potential benefit of vertically sampling a mixed-phase environment at multiple mesonet sites and highlights future scientific and operational questions to be addressed by the UAV community.

KEYWORDS: Winter/cool season; Freezing precipitation; Mixed precipitation

1. Introduction

In the southern Great Plains (SGP; Oklahoma and Texas), winter weather can have large societal and economic impacts due to heavy ice loading, power outages, travel disruptions, and low predictability in precipitation-type forecasts (Changnon 2003; Ralph et al. 2005; Call 2010). Despite the fact that other regions of the United States have more frequent winter storms, disaster declarations and monetary federal aid for winter storms is typically highest in the SGP (Changnon 2003; Changnon and Karl 2003; Changnon et al. 2006; Grout et al. 2012), with nearly 50% of all ice storms and 30% of all blizzards resulting in a disaster declaration in Oklahoma (Grout et al. 2012). Meteorologically, this is because SGP ice storms are typically associated with long-duration (>12 h) icing and abundant moisture (Rauber et al. 2001; Changnon 2003), leaving this geographic region at increased risk for high-impact ice storms.

It has been shown that mesoscale processes and boundary layer characteristics are extremely important as they can alter the precipitation type (Thériault et al. 2010; Reeves et al. 2014; Stewart et al. 2015). For example, Thériault et al. (2010) showed that perturbations in the vertical profile as small as 0.5°C can result in a different precipitation type being observed at the surface. In addition to vertical variability, Reeves (2016) points out that horizontal variability in precipitation type found in nature can occur on subgrid scales for high-resolution convection-allowing models. With respect to temporal resolution, most ice pellet and freezing rain events typically have durations less than half an hour (Reeves 2016), suggesting that once-hourly analyses are inadequate to capture the actual evolution of the surface hydrometeor phase. This variability leads to complex situations in which discriminating hydrometeor type becomes one of the leading problems for winter-weather prediction.

Despite advancements in numerical weather prediction and precipitation-type algorithm development, forecasting accuracy is still a great challenge in the SGP region (Ikeda et al. 2017; McCray et al. 2019). Previous studies have utilized ground-based and remote-sensed observations synthesized with NWP models, crewed aircraft, and radiosondes to gain an understanding of the evolution of the atmosphere. However, studies suggest that despite the current observational network, the lower levels of the atmosphere (specifically the PBL), are not properly sampled, potentially leaving out important details that could improve our scientific understanding of winter weather and forecasting ability (NRC 2009; Moore 2018; Chilson et al. 2019).

Currently, radiosondes are the primary source through which the meteorological community obtains high-resolution PBL measurements. However, there are a few caveats associated with radiosonde measurements. Because balloons drift in the wind, these measurements are not true vertical profiles and, hence, may not sample the path taken by hydrometeors. When dealing with winter-weather environments involving high horizontal variability, this amount of drift may lead to disagreements between the diagnosed precipitation phase and what is actually observed. Additionally, measuring at high temporal frequencies can be very costly as the instrumentation is typically not recoverable and each launch usually requires a dedicated workforce. The current radiosonde network density is not always suitable to represent the horizontal variability associated with mixed-phase winter weather discussed in Reeves et al. (2014) and Reeves (2016).

Corresponding author: David L. Boren, daniel.tripp@noaa.gov

TABLE 1. Technical specifications of weather sensors used in this experiment. Radiosonde metrics listed are manufacturer specifications. UAV metrics were calibrated/validated by CASS on the full integrated UAV system.

	UAV		Radiosonde iMet-4	
	Temperature iMet-XF PT-100	Humidity HYT-271	Temperature	Humidity
Sensing element	Bead thermistor	Capacitor	Bead thermistor	Capacitive polymer
Range	From +50 to −90°C	0%–100%	From +60 to −90°C	0%–100%
Response time	≤2.7 s[a]	≤4.5 s[a]	≤1 s (at 5 m s^{-1})	5.2 s (at 5°C)
Resolution	0.01°C	0.1%	0.01°C	0.1%
Sampling rate	20 Hz	20 Hz	1 Hz	1 Hz

[a] At 12 m s^{-1} from onboard fan and $T = 0$°C

Several researchers have begun implementing uncrewed aerial vehicles (UAVs) as a cost-efficient and highly versatile solution to filling data gaps in the PBL (Reuder et al. 2008; Elston et al. 2011; Houston et al. 2012; Cassano et al. 2016; de Boer et al. 2016; Koch et al. 2018; Jacob et al. 2018; Greene et al. 2018; Moore 2018; Chilson et al. 2019; Greene et al. 2019; Bell et al. 2020; de Boer et al. 2020; Segales et al. 2020; Pillar-Little et al. 2021). The emerging technology of UAVs has become a reliable platform for measuring state variables at fine scales in the atmosphere and is in the beginning stages of being implemented into a statewide 3D mesonet in Oklahoma (Chilson et al. 2019). Warm-season studies of UAVs has been the primary focus in the last decade. Less effort has been devoted to assessing UAV utility for the cool season, with previous studies focusing on measuring Artic and Antarctic environments and not necessarily during active precipitation (Curry et al. 2004; Inoue et al. 2008; Cassano et al. 2016; de Boer et al. 2018).

This study employs UAVs as a new observational tool to provide insight into winter-weather processes in an Oklahoma mixed-phase environment. UAV vertical profiles of active winter precipitation that were collected in February 2019 are compared to the local observational network, as well as model analyses and precipitation-type algorithm output. This study examines the impact of high-resolution observations for one case study and is intended as a "proof of concept" for future studies to build upon. Suggestions for UAV applications in winter weather and insights on how this new technology can be utilized alongside the current observational network as a 3D mesonet are presented herein.

The UAV discussion in this paper is organized into three sections. Section 2 outlines all of the observational and model data utilized in this study. Section 3 utilizes low-level UAV vertical profiles of temperature and relative humidity along with radiosondes to diagnose precipitation type at a point location in central Oklahoma. Section 4 explores how a network of UAVs could sample a mixed-phase environment at different point locations within the state and also introduces important scientific and operational questions to address in future studies.

2. Data and methods

a. UAVs

The CopterSonde 2.5 rotary-wing UAV developed by the Center for Autonomous Sensing and Sampling (CASS) at the University of Oklahoma (OU) is utilized for gathering atmospheric data in winter weather. The sensor payload is housed inside a custom 3D printed shell on the front of the quadcopter. A fan draws air inside an L-shaped duct and across the sensors to ensure proper sampling and to protect the sensors from solar radiation. The technical specifications and details regarding atmospheric measurement integrity can be found in other literature (Greene et al. 2018; Barbieri et al. 2019; Greene et al. 2019; Bell et al. 2020; Segales et al. 2020) and in Table 1. In general, previous studies conclude that the CopterSonde performs well when compared to other in situ measurements (temperature and relative humidity), primarily because of sun shielding and appropriate airflow around sensors.

Because all previous testing was conducted in fair weather conditions, sensor integrity during icing conditions has not been characterized for this platform and is one important caveat to note for this experimental dataset. Waugh and Schuur (2018) found that icing on radiosondes can impact sensor response time and produce incorrect measurements. During the event studied herein, there was evidence of icing on the rotors and the outer shell. Between flights the UAV and sensor package were inspected for icing and dried off to avoid sensor wetting. No in-flight deicing measures were implemented on this platform and the authors note the importance of icing mitigation for flight performance and sensor integrity. To mitigate potential icing contamination, data were manually quality controlled by identifying any nonphysical signature or strong bias in relation to other observations in the vertical profile.

b. Radiosondes

iMet-4 radiosondes were utilized during this field experiment to capture the vertical profile beyond the flight ceiling of the UAV. Four radiosondes were launched; however, due to evidence of sensor icing in the last two launches, only surface observations are obtained from the final two soundings for this study. Each of the radiosondes are displaced at least 10 min in time from UAV profiles to ensure the platforms did not collide during flight. Technical specifications of sensor integrity are found in Table 1.

c. Oklahoma Mesonet

The Oklahoma Mesonet is composed of a network of 120 stations that relay weather and soil observations at a high temporal frequency (Brock et al. 1995; McPherson et al. 2007).
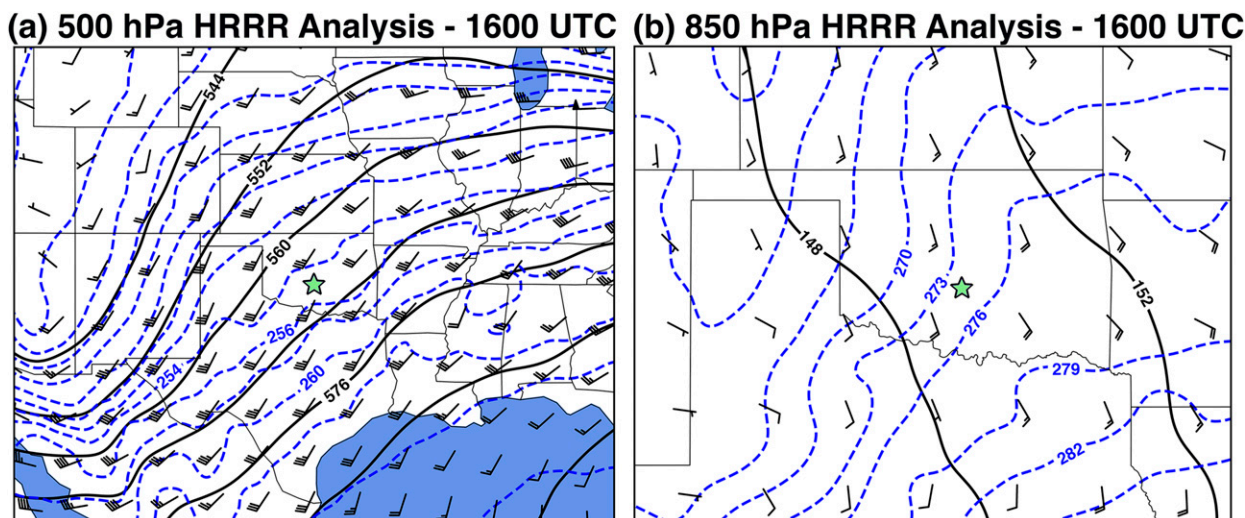
FIG. 1. The 1600 UTC HRRR analysis of (a) 500- and (b) 850-hPa geopotential heights (solid black; dam), isotherms (dashed blue; K), and winds [black barbs; kt (1 kt ≈ 0.51 m s^{-1})]. In this and all subsequent figures, the UAV flight location (KAEFS) is denoted with a green star.

There is at least one station in every Oklahoma county measuring temperature, relative humidity, wind, solar radiation, precipitation, and pressure. Postprocessed data are collected from the Oklahoma Mesonet's archive in 30-min intervals and a cubic interpolation is employed in between stations for analysis of the surface temperature for the winter-weather event studied herein.

d. Other surface observations

Additional surface observations are obtained from the Automated Surface Observing System (ASOS; National Weather Service 1998), Automated Weather Observing System (AWOS), and Meteorological Phenomena Identification Near the Ground (mPing; Elmore et al. 2014). ASOS and AWOS directly observe precipitation type at given locations and report subhourly data. mPing observations are crowd-sourced observations of precipitation type collected by the general public. Details regarding their accuracy and usage can be found in other studies (Reeves et al. 2014; Elmore et al. 2015; Reeves 2016; Burg et al. 2017; Ikeda et al. 2017).

e. High-Resolution Rapid Refresh model

The High-Resolution Rapid Refresh (HRRR) model is a convection-allowing model with a 3-km grid as well as 3-km radar assimilation (Benjamin et al. 2016; Alexander et al. 2017). The HRRR assimilates data from several observational networks (mesonet, ASOS, radar, etc.) including the Oklahoma Mesonet. A backward–forward two-pass digital-filter initialization process is applied to incorporate microphysics at initialization (for more details, see Benjamin et al. 2016). The analysis data used herein are interpolated to pressure coordinates with a vertical spacing of 25 hPa. During the winter event studied herein, a surface-based subfreezing layer was capped by a single warm layer ($T > 0$°C) aloft. This paper defines the elevated warm layer ($T > 0$°C) as the vertical area bounded by

the bottommost and topmost crossings of the 0°C isotherm. It is possible to have multiple crossings of the 0°C isotherm, however, this method captures the depth of all potential melting layers.

3. Results

a. Mesoscale analysis

On 19 February 2019, OU CASS deployed the CopterSonde to measure winter precipitation in central Oklahoma. The Kessler Atmospheric and Ecological Field Station (KAEFS; see Fig. 1 for location), located in Washington, Oklahoma, is the base for UAV operations and is a designated OU location where UAVs can fly above the regular flight ceiling laid out by a Certificate of Authorization (COA) granted from the Federal Aviation Administration (FAA). All UAV flights and radiosonde launches are collocated with the Washington mesonet tower in this study.

On the morning of 19 February, southerly isentropic lift inferred from Fig. 1 developed over a cold-frontal surface and produced precipitation over most of Oklahoma (Figs. 1 and 2). At 1600 UTC, the composite reflectivity (Fig. 2a) depicts light precipitation moving into central Oklahoma. However, base reflectivity scans (0.5–0.75 km AGL; KTLX) indicate no echo, suggesting subcloud evaporation. This results in cooling near the surface and an increased thickness of a preexisting surface-based subfreezing layer (not shown). Precipitation at KAEFS is first observed at the surface at 1630 UTC (Fig. 2b) as ice pellets. By 1700 UTC (Fig. 2c), the precipitation type transitions to liquid at KAEFS. In northwest Oklahoma, a snowband (Fig. 2) produces about 19 cm (7.5 in) of snow in Burlington, OK (225 km northwest of KAEFS). Trace amounts of winter precipitation are observed outside of the snowband in areas of weaker echo indicated in Fig. 2 (not shown).
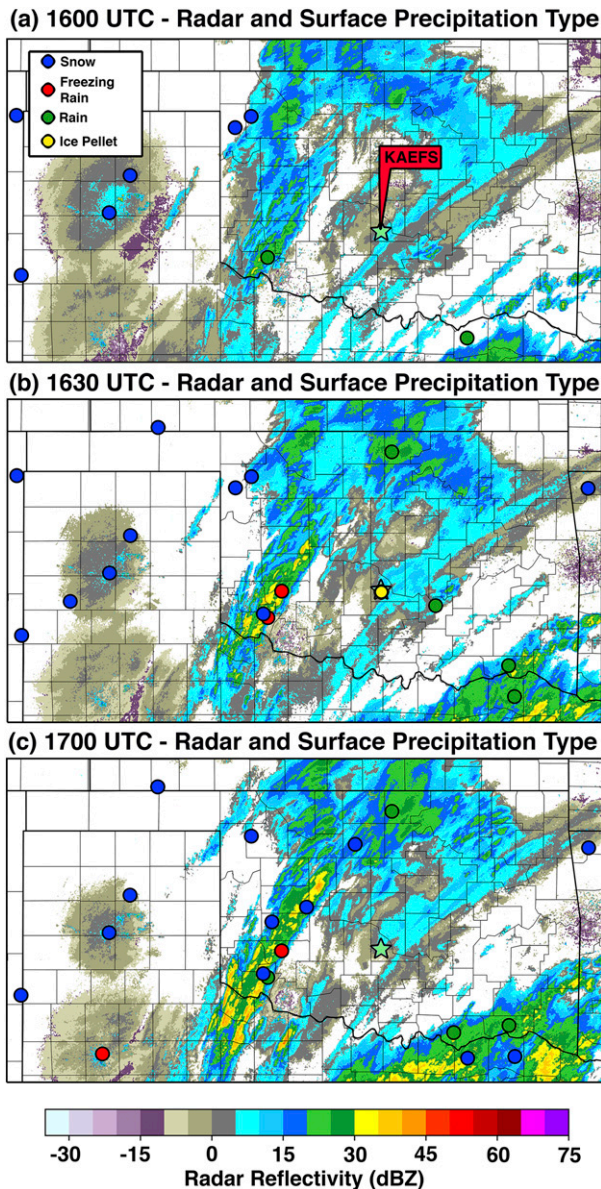
FIG. 2. The Multi-Radar Multi-Sensor (Zhang et al. 2016) composite radar reflectivity prior to quality control (to maintain valid echo; Reeves and Waters 2019) at (a) 1600, (b) 1630, and (c) 1700 UTC 19 Feb 2019. ASOS/AWOS/mPing precipitation-type observations from the previous 30 min are overlaid in colored circles as indicated in the legend of (a).

To gain an understanding of the horizontal and vertical structure of the atmosphere surrounding KAEFS, the Oklahoma Mesonet and the HRRR analyses are utilized. Southerly warm advection leads to the formation of an elevated warm layer ($T > 0°C$) throughout the day on 19 February. Figure 3 depicts the location and thickness of the elevated warm layer along with surface observations of precipitation type. The 0°C isotherm for the HRRR and the mesonet (Fig. 3) indicates a southwest/northeast oriented boundary throughout the event.

At 1200 UTC (Fig. 3a), a deep elevated warm layer caps a surface-based subfreezing layer whose temperature hovers near 0°C. Northwest of the 0°C isotherm, the depth of the warm layer decreases and eventually erodes completely. As precipitation forms in central Oklahoma, the surface 0°C isotherm moves to the southeast (Figs. 3b,c) possibly due to latent cooling associated with melting. This cold-air intrusion creates a transition zone throughout central Oklahoma with an elevated warm layer that is about 1500 m deep. This leads to a favorable environment for mixed-phase hydrometeor formation (Figs. 3b,c). By 2000 UTC (Fig. 3d), surface observations indicate a broad precipitation shield across the state with some mixed precipitation in central Oklahoma.

The HRRR surface temperature is compared with the mesonet analysis (Fig. 3). There are some local nuances that are marginally different between the two analyses (bias < 2°C). These are consistent with those found in previous investigations (Ikeda et al. 2017). Additionally, the HRRR does not fully capture the magnitude of the surface-based refreezing layer, which is discussed in section 3b. However, the general weather pattern and progression captured by the HRRR of the 19 February case study does agree with the observations. Figure 4 shows a time–height cross section of the HRRR vertical temperature profile at KAEFS. As precipitation moves into KAEFS (1600 UTC), the refreezing layer near the surface deepens and cools, and the melting layer begins to cool as precipitation intensity increases. This pattern has been found by McCray et al. (2019) to be the common setup for mixed-phase precipitation in the southern plains.

b. KAEFS in situ UAV and radiosonde observations

We now consider the UAV and radiosonde observations taken during this event. Data collection begins before sunrise (1312 UTC) at 1200 UTC with light surface winds and cloudy skies. Winter precipitation moves in at 1630 UTC in the form of ice pellets (Fig. 2). Precipitation type transitions to rain by 1700 UTC and continues intermittently until data collection concludes at 2030 UTC. Throughout the entire study period, the surface temperature is around 0°C ($\pm 1°C$; as seen in Fig. 5a) resulting in periods of intermittent freezing rain and rain. Additionally, the wet-bulb temperature (T_w; Fig. 5b) is subfreezing at 1630 UTC but edges close to 0°C in subsequent hours. No icing is observed across the land surface at KAEFS; however, elevated exposed surfaces and objects (antenna equipment, cables, tree branches) have small amounts of ice accretion visible during the study period.

The UAV is programmed to ascend vertically at $3 \, \mathrm{m \, s^{-1}}$ and obtain temperature and relative humidity measurements every second up to a maximum flight ceiling of 1500 m AGL. Vertical profiles are gathered from 1200 to 2000 UTC with a total of 18 flights at 15–30 min intervals on average. As flights in active winter precipitation have never been tested on this aircraft, the temporal resolution varies throughout the study period as weather conditions (primarily icing) impact flight performance. Additionally, the flight ceiling is limited throughout the study because of icing, high winds, and visibility constraints laid out by the FAA. Like the UAVs, ascent rates for the radiosondes

(a) 1200 UTC

(b) 1600 UTC

(c) 1700 UTC

(d) 2000 UTC

Legend:
- Snow (blue)
- Freezing Rain (red)
- Rain (green)
- Ice Pellet (yellow)

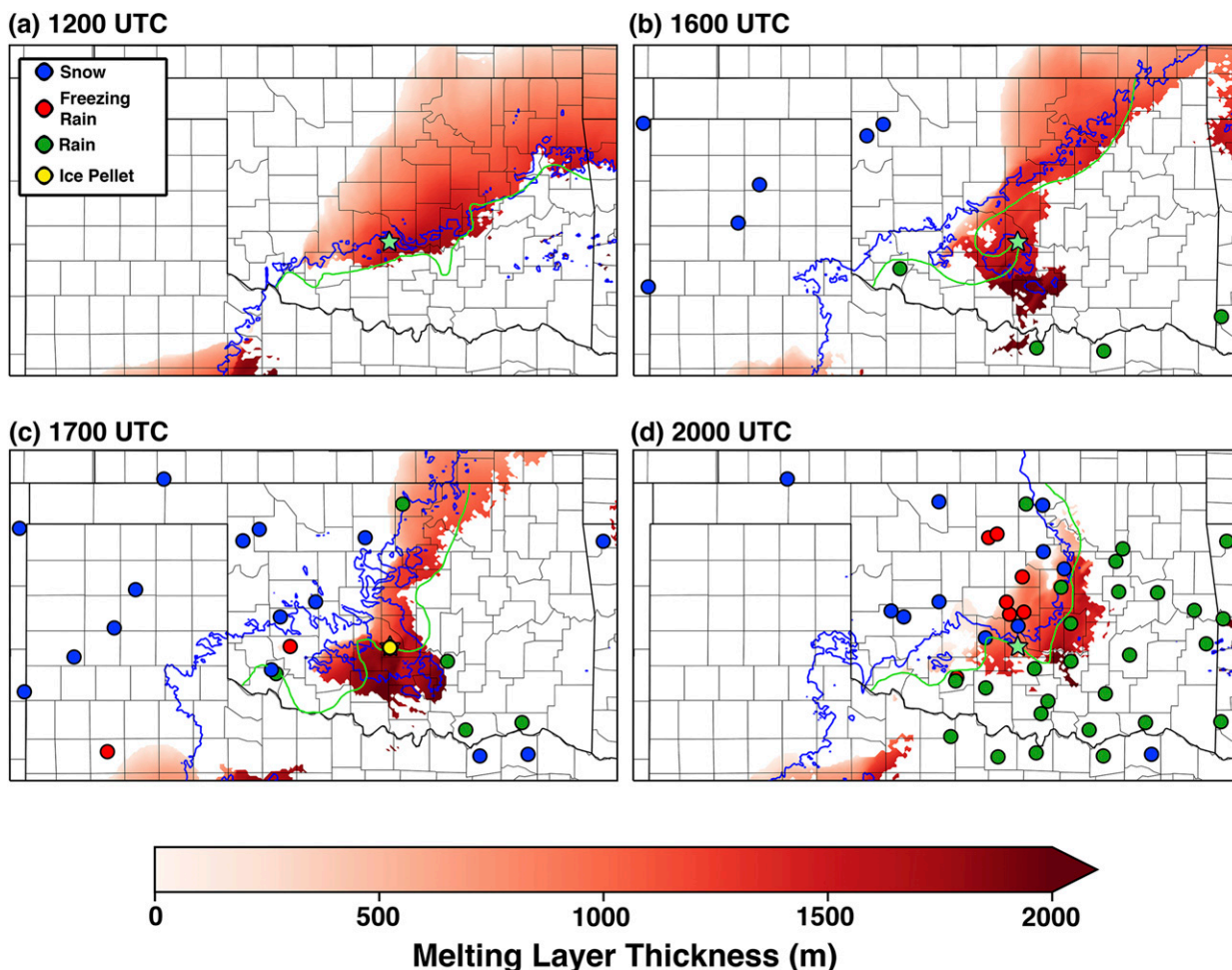Melting Layer Thickness (m)
0 500 1000 1500 2000

FIG. 3. The HRRR analysis of the depth of the elevated warm layer (shaded) and location of the surface 0°C isotherm (blue), along with a manual analysis of the surface 0°C isotherm using observations from the Oklahoma Mesonet (green), at (a) 1200, (b) 1600, (c) 1700, and (d) 2000 UTC 19 Feb 2019. The UAV flight location (KAEFS) is denoted with a green star. ASOS/AWOS/mPing precipitation-type observations from the previous hour are overlaid in colored circles as indicated in the legend of (a).

are also $3\,\mathrm{m\,s}^{-1}$ in the PBL and launched (1230, 1630 UTC) near UAV flight times.

At 1200 UTC, four hours before precipitation begins, radiosonde and UAV measurements indicate a surface-based refreezing layer around 650 m deep (Fig. 6a). The observations agree within ±1°C with the HRRR analysis temperature profile in the lower 650 m. The largest difference between the observations and the model occurs in the melting layer aloft with the radiosonde recording 2°C warmer than the HRRR at 800 m (Fig. 6b).

By 1630 UTC (Fig. 6c), evaporative cooling is evident in the lowest kilometer of the atmosphere as the 700 m temperature (approximate height of base reflectivity scans) cools to −5.1°C and the surface-based refreezing layer grows up to 1050 m in the radiosonde data. The same degree of cooling is not captured by the HRRR (Fig. 6d). Both the UAV and radiosonde are up to 3°C colder between 342 and 972 m AGL (Fig. 6d). This cooling of the refreezing layer is sufficient to lead to the formation of ice pellets, consistent with what previous

investigations have found (Thériault et al. 2010; Reeves et al. 2014; Stewart et al. 2015).

Time–height cross sections of temperature show that both UAV observations and the HRRR have similar characteristics from 1200 to 1300 UTC (Figs. 7a,b). As precipitation approaches (around 1500 UTC), the surface-based refreezing layer becomes a few degrees colder in the observations (Fig. 7b) relative to the HRRR (Fig. 7a; also seen in Fig. 6d). A similar cold pocket develops in the HRRR but is delayed in time until 1800 UTC (Fig. 7a). Additionally, as precipitation moves over KAEFS (1600–2000 UTC), T_w (Figs. 7c,d) begins increasing as the PBL becomes saturated from intermittent precipitation (also seen at the surface in Fig. 5b).

The UAV and radiosonde observations in Figs. 6 and 7 display complementary evidence of a refreezing layer that is around 1 km thick, leading to the production of ice pellets at 1630 UTC. The primary characteristic that sets UAVs apart, is that they are able to capture the evolution of the PBL on much higher temporal scales than the HRRR or the operational
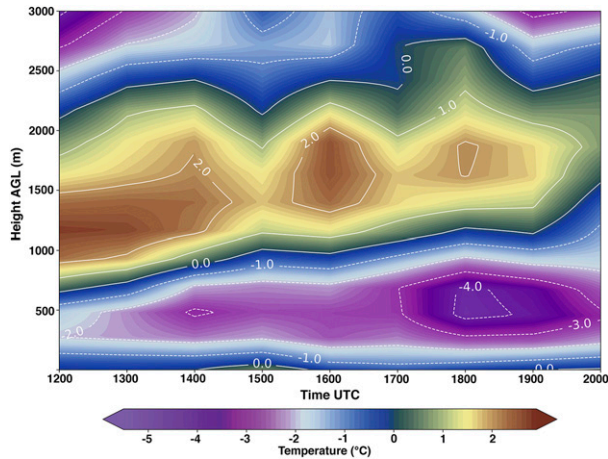
FIG. 4. The HRRR time–height cross section of temperature at KAEFS during the 19 Feb 2019 winter-weather case study. Solid contours denote values above 0°C, and dashed contours are values below 0°C.

radiosonde network. Table 2 provides a summary of the melting-/refreezing-layer thicknesses from each of the different datasets. Primarily, the HRRR captures the thicknesses of the melting and refreezing layers well. The largest discrepancy is in the temperature of the subcloud layer, wherein the HRRR is 3°C warmer than the UAV and radiosonde suggest. This may be due to inadequate representation of evaporative cooling in the HRRR, but an exact diagnosis of the cause is outside the

scope of this work. The UAV data illustrates that in situ observations collected on hourly to subhourly temporal scales, can add valuable information about the vertical structure of the atmosphere alongside the radiosonde network in Oklahoma.

c. Impacts on surface precipitation-type

Are the differences between the HRRR and the UAVs significant enough to affect the diagnosis of hydrometeor phase? This question is answered by utilizing the spectral-bin classifier (SBC; Reeves et al. 2016). The SBC is a precipitation-type algorithm that calculates the liquid-water fraction of hydrometeors across a given drop size distribution (DSD) to determine the surface precipitation type (Reeves et al. 2016). The algorithm is able to diagnose six different categories of precipitation (rain, snow, rain–snow mix, freezing rain, ice pellets, and a freezing rain–ice pellet mix) by analyzing a given temperature and relative humidity profile.

The SBC is sensitive to the ice-nucleation temperature (T_{ice}). Reeves et al. (2016) found T_{ice} of −6°C to be the most statistically robust but noted that other thresholds are scientifically valid and may, in fact, be more appropriate in certain situations. Another study (Thompson et al. 2014) utilized T_{ice} of −4°C. Because of this uncertainty, a range of T_{ice} (from −6° to −2°C) is employed herein to assess the impacts of temperature/humidity differences between the UAV, radiosonde, and HRRR on hydrometeor phase.

Figure 8a shows the vertical T_w profile with the associated hydrometeor phase for the 1600 UTC HRRR analysis. All precipitation phase diagrams for the HRRR (Fig. 8a; for T_{ice} of −6° and −5°C) show complete melting of all bin sizes in the
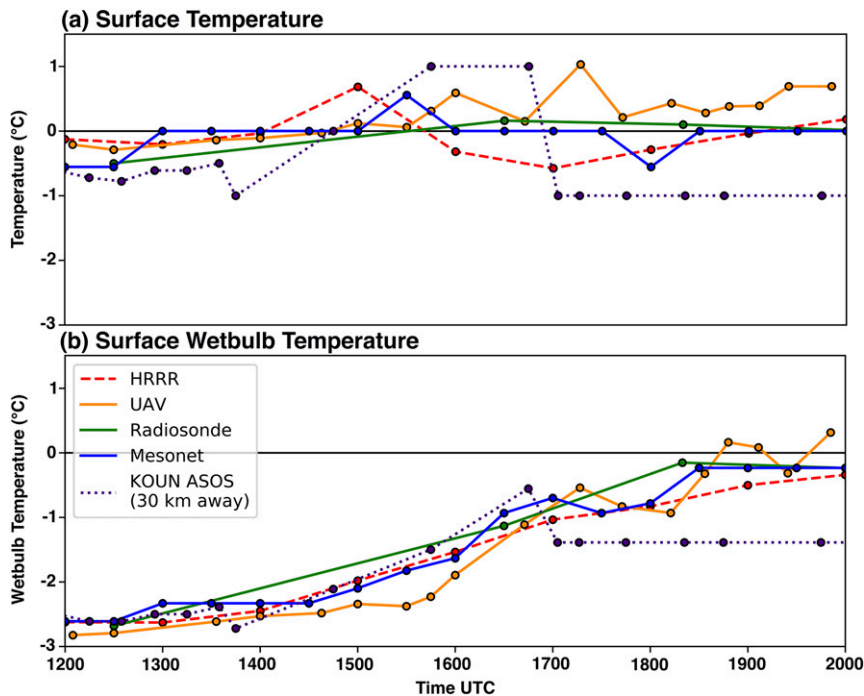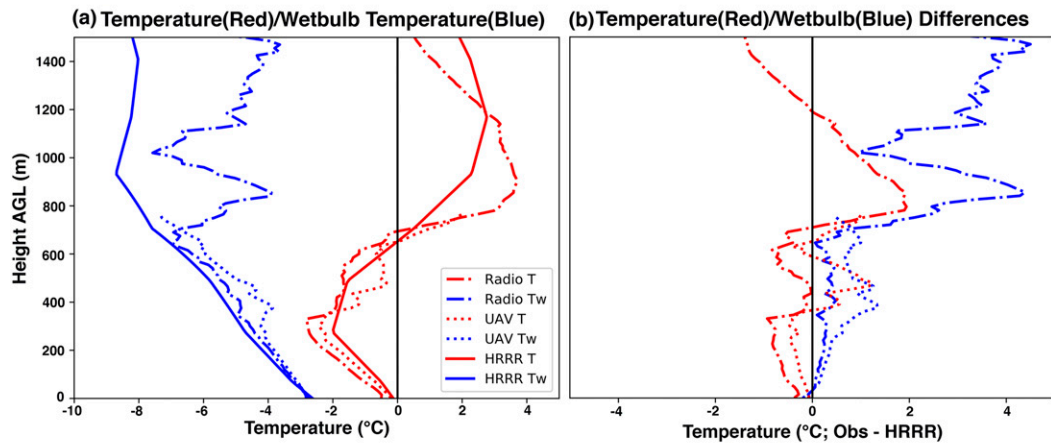

FIG. 5. Observed/analyzed surface (a) temperature and (b) wet-bulb temperature on 19 Feb 2019; 0°C is denoted by a horizontal black line.
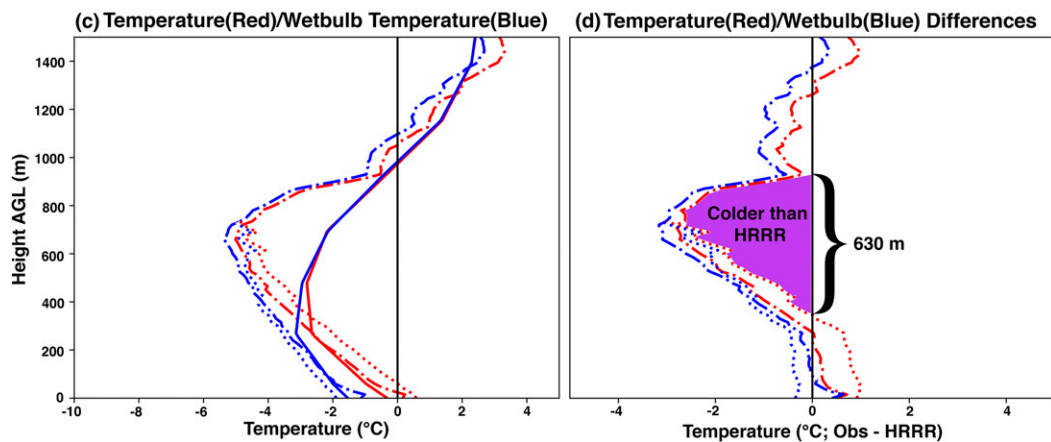
FIG. 6. KAEFS data collected on 19 Feb 2019. (a) Vertical profiles of temperature (red) and wet-bulb temperature (blue) from the 1200 UTC HRRR analysis (solid), 1205 UTC UAV flight (dotted), and 1230 UTC radiosonde (dot–dashed). (b) Vertical profiles of observational temperature (red) and wet-bulb temperature (blue) differences from the HRRR analysis at the same observational times as in (a). (c) As in (a), but for the 1600 UTC HRRR analysis, 1600 UTC UAV flight, and 1630 UTC radiosonde. (d) As in (b), but for the 1600 UTC UAV flight and 1630 UTC radiosonde.

elevated warm layer before they encounter the surface-based subfreezing layer. This results in a surface classification of freezing rain/drizzle. One would need to increase T_{ice} to $-2°C$ (not shown)—an unrealistic threshold for ice nucleation—in order for this profile and algorithm to result in an ice pellet diagnosis.

Figure 8b illustrates the same analysis, but for the 1630 UTC radiosonde launched during ice pellet precipitation. The T_w profile looks similar to the HRRR (Fig. 8a) except the refreezing layer is colder by $3°C$ (also seen in Fig. 6d). For T_{ice} of $-6°C$, we see the same surface classification as the HRRR: freezing rain/drizzle. However, when T_{ice} is less than or equal to $-5°C$, the phase diagram illustrates a shallow layer of supercooled liquid (freezing rain/drizzle) transitioning to ice pellets around 750 m. This results in a surface classification of ice pellets, which corroborates what is observed at KAEFS.

Additionally, as shown in Fig. 6, UAVs can provide insight into the lower-level thermodynamic structure. Figure 8c incorporates the 1600 UTC UAV data; however, this profile is capped by a 750 m flight ceiling. Therefore, the rest of the vertical profile is populated by the 1600 UTC HRRR (Fig. 8a). The surface classifications for T_{ice} at $-6°C$ and T_{ice} at $-5°C$ are identical to the radiosonde data (Fig. 8b) and depict a shallow supercooled liquid layer capping a layer with ice pellets. These data highlight how small differences in the thermodynamic structure between the model and the observations on 19 February impact the surface classification of precipitation type. Figure 8 additionally illustrates the strengths UAVs have in collecting low-level thermodynamic measurements identical to radiosondes. However, it is evident that measurements at higher altitudes are needed to provide enough information for precipitation-type algorithms to produce a meaningful classification.
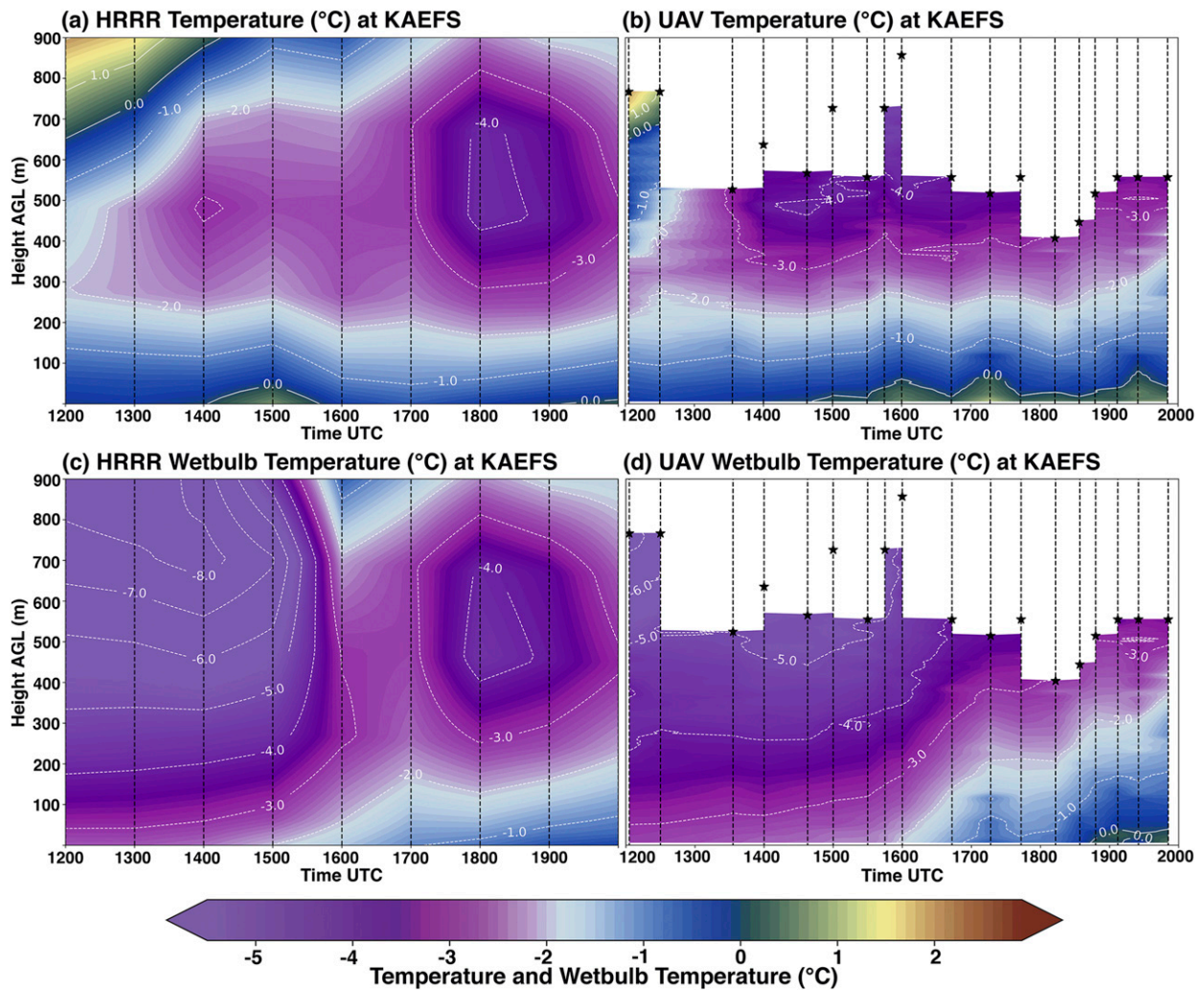
FIG. 7. Plots of time (UTC) vs height (m) at KAEFS on 19 Feb 2019. (a) HRRR temperature (°C) as in Fig. 4, but confined to the lowest 900 m. Sampling frequency is denoted by the dashed vertical lines. (b) UAV temperature (°C). Vertical profiles are denoted by dashed vertical lines, with flight ceilings marked with stars. (c) HRRR wet-bulb temperature (°C). Sampling frequency is denoted by the dashed vertical lines. (d) As in (b), but for wet-bulb temperature. Solid contours denote values above 0°C, and dashed contours are values below 0°C.

4. Future operational and scientific objectives learned from simulated UAV data

Assessing the efficacy of UAVs for winter weather in Oklahoma is logistically challenging for a number of reasons. Mixed-phase events do not commonly occur in Oklahoma and when they do, there is no guarantee the weather will be centered on the top of designated FAA flight locations. Field campaigns and the operational costs of collecting these types of data are expensive and require large teams. Because of these costs, it is not feasible to test different configurations of a UAV network at local mesonet sites. These constraints restrict the ability to do cross comparisons of different network configurations that are free from possible influences from different weather patterns.

TABLE 2. Summary of melting- and refreezing-layer thicknesses. The lowest 50 m are ignored when defining the refreezing layer.

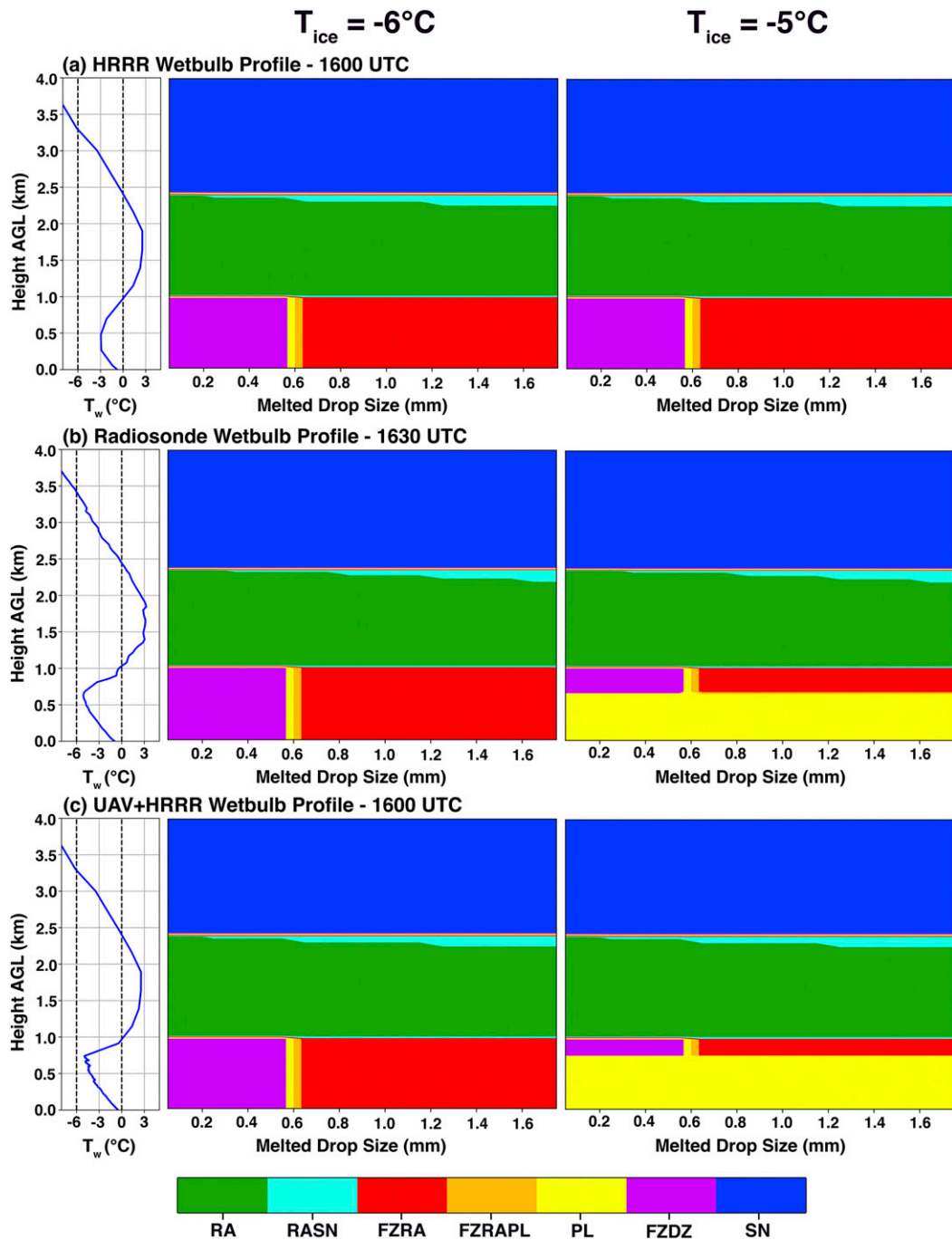|	HRRR melt layer	Radiosonde melt layer	HRRR refreezing layer	Radiosonde refreezing layer	UAV refreezing layer
1200 UTC	1462 m		651 m		645 m
1230 UTC		1578 m		675 m	662 m
1600 UTC	1471 m		972 m		>750 m
1630 UTC		1497 m		1050 m	>500 m
1700 UTC	1109 m		1074 m		>500 m
2000 UTC	913 m		1560 m		>520 m

FIG. 8. Wet-bulb temperature profiles with the associated hydrometeor phase at an ice nucleation temperature of (left) −6° and (right) −5°C for the (a) 1600 UTC HRRR analysis, (b) 1630 UTC radiosonde, and (c) 1600 UTC HRRR/UAV hybrid profile. The profile in (c) is composed of UAV data in the lower 750 m and HRRR data in the upper levels. Classification abbreviations are as follows: RA = rain, FZRA = freezing rain, PL = ice pellet, FZDZ = freezing drizzle, SN = snow, or a mixture of these types.

In an effort to overcome these constraints, this section illustrates how multiple UAVs in a 3D network could sample a winter-weather environment and highlights operational and scientific questions that need to be addressed in future work. A modeling study is undertaken as a cost-effective way to create synthetic observations for illustrative purposes. This task can be accomplished by any mesoscale model such as the HRRR, but this study utilizes the Advanced Research version of the Weather Research and Forecasting (WRF-ARW) Model (Skamarock et al. 2019) in an effort to simulate subhourly

FIG. 9. Domain layout for the numerical simulation experiment. The horizontal grid spacings for domains 1 (black outline) and 2 (blue outline) are 3 and 1 km.

data similar to a potential UAV sampling frequency. Synthetic UAV data generated in this study are intended as a proof-of-concept demonstration to provide a foundation for future efforts seeking to comprehensively pin down the efficacy of a 3D UAV network.

The WRF simulation is conducted for the same event (19 February 2019) discussed in section 3 and initialized with the HRRR analysis data. Two domains are utilized with a horizontal grid spacing of 3 and 1 km, respectively (as outlined in Fig. 9 and Table 3). All parameterizations closely mirror those utilized in the HRRR. The results of the simulation are comparable to the differences pointed out in section 3 between the observations and the HRRR (not shown). Additional details regarding the simulation parameterizations can be found in Table 3.

The 3D mesonet concept discussed in Chilson et al. (2019) proposes the implementation of a semiautonomous UAV network stationed at existing mesonet sites. To further explore

what could be observed if such a network were operational during a mixed-phase environment, locations A, B, C, and D (actual mesonet sites) in Fig. 10 are analyzed herein.

WRF analysis

The SBC precipitation-type algorithm is run across the WRF domain and highlights a transition zone extending through central Oklahoma (Fig. 10). Looking through both time and space, Figs. 10a–c shows that mesoscale variability is captured in this simulation and represents a mixed-phase environment as observed in nature. From a UAV perspective, there are several fine-scale features in Fig. 10 that could have notably different thermodynamic profiles.

As an exercise in extracting synthetic data and assuming perfect instrumentation without error or hysteresis, UAV profiles of T_w at locations A–D are provided in Fig. 11. A 15-min sampling frequency is denoted by dashed vertical lines to simulate data collection at this frequency. Location A (Fig. 11a) is the northernmost station on the coldest side of the transition zone. A shallow and weak elevated warm layer (Fig. 11a) results in partial melting of only the smallest hydrometeors. The majority of hydrometeors remain frozen through this layer, leading to the snow classification noted in Fig. 10. However, location B (Fig. 11b) favors mixed-phase precipitation from 1800 to 1945 UTC due to melting at 2 km with T_w primarily warmer than T_{ice} in the refreezing layer. Location C (Fig. 11c) is similar to location B, except there is more evidence of melting, thus trending toward more liquid forms of precipitation instead of mixes at the surface.

Location D (Fig. 11d) is more characteristic of a liquid-precipitation environment due to its warm melting layer and a refreezing layer primarily warmer than T_{ice} from 1715 UTC onward. One unique characteristic of location D highlighted in Fig. 10b is the rapid transition to snow at 1900 UTC. One hypothesis for this rapid cooling is that precipitation loading cools the environment as well as adds moisture resulting in T_w decreasing by 4°C (Fig. 11d). Thus, the surface classification transitions from rain to a rain–snow mix in 30 min.

TABLE 3. Design of WRF-ARW numerical weather prediction system for a real data case on 19 Feb 2019. Domain locations [domains 1 (d01) and 2 (d02)] are laid out in Fig. 9.

Model settings	
Horizontal grid spacing	d01 = 3 km; d02 = 1 km
Vertical levels	80
Initial conditions	3-km HRRR
Boundary conditions	3-km HRRR
Start time	0000 UTC
End time	2100 UTC
Output frequency	d01 = hourly; d02 = 15 min
Physics settings	
Cumulus convection	None
Boundary layer	MYNN 2.5-level TKE scheme (Nakanishi and Niino 2006)
Surface layer	MYNN surface layer (Nakanishi and Niino 2006)
Microphysics	Thompson (Thompson et al. 2008)
Land surface	RUC land surface model (Smirnova et al. 2016)
Longwave radiation	RRTMG scheme (Iacono et al. 2008)
Shortwave radiation	RRTMG scheme (Iacono et al. 2008)

(a) 1800 UTC - WRF Surface Precipitation Type

(b) 1900 UTC - WRF Surface Precipitation Type

(c) 2000 UTC - WRF Surface Precipitation Type

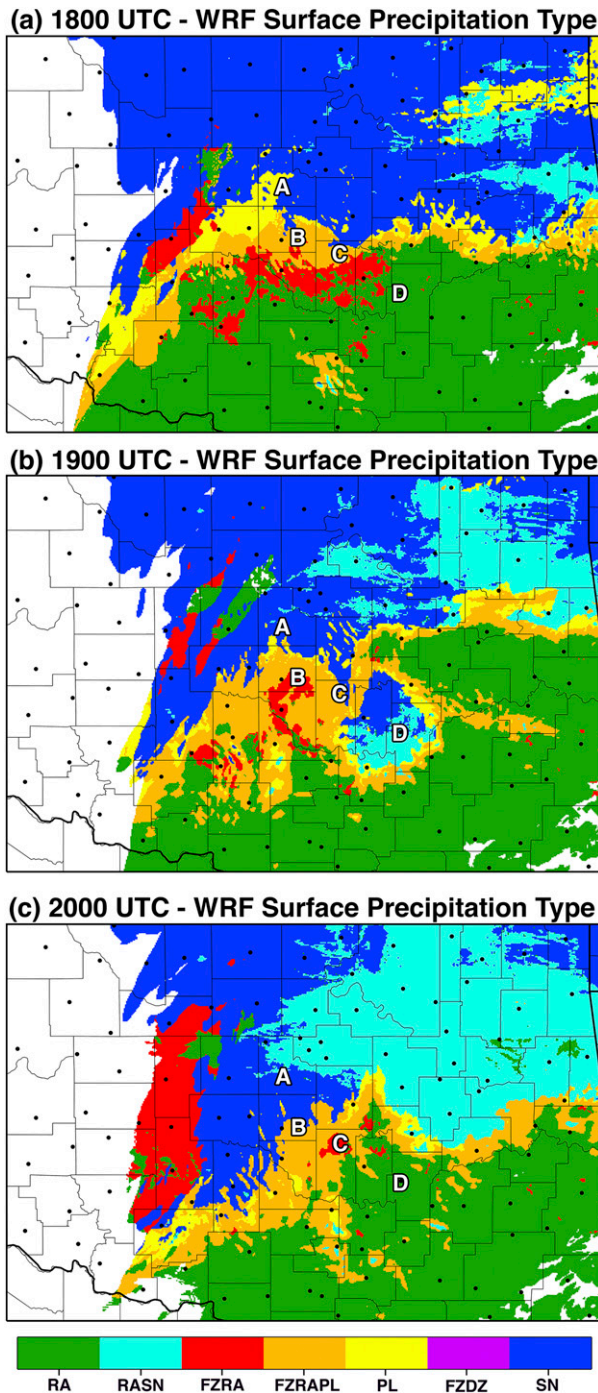| RA | RASN | FZRA | FZRAPL | PL | FZDZ | SN |

FIG. 10. WRF-simulated surface precipitation type (SBC) of the 19 Feb 2019 Oklahoma winter storm at (a) 1800, (b) 1900, and (c) 2000 UTC. Oklahoma Mesonet locations are denoted with black dots. Four mesonet sites (A, B, C, and D) perpendicular to the transition zone are highlighted for this study.

These observations illustrate what could be captured by a hypothetical network of UAVs stationed at local mesonet sites. Looking through the lens of data assimilation, low-level observations are not captured on these scales from the operational

radiosonde network. Reeves et al. (2014) points out that precipitation-type forecasts are more sharply influenced by the initial conditions of a model as opposed to forecast lead time suggesting that observations such as this may be beneficial. However, future observing system simulation experiments (OSSEs) are needed to explore if a network such as this could improve high-resolution NWP. It is important to note that a general survey of Fig. 10 indicates that even if a UAV were stationed at every mesonet site, there would still possibly be gaps in capturing the mesoscale variability present in the simulation. This brings to question how many UAV sites are necessary to improve winter forecasts if any improvement at all. Studies involving different UAV network configurations along fine-scale mesoscale features such as the one presented in Fig. 10 are encouraged in future work.

This dataset also provides guidance on target flight ceilings needed to capture useful information. Flights targeted at a 1-km flight ceiling can capture the magnitude of the refreezing layer, which could help discriminate ice pellets (Fig. 11). However, melting-layer data are required to discriminate mixes and all other forms of precipitation. This case suggests that flights would need to ascend to 3 km, but clearly this is just one event. If this exercise were repeated for an entire season or with similar cases, an accurate concept of operational requirements could be proofed for future field campaigns. Additionally, future modeling studies need to explore these target flight ceilings in context of cloud bases. The FAA requires most UAV operations to maintain visual line-of-sight (VLOS), which could greatly impede future UAV winter weather field campaigns with low cloud bases.

Figure 11 depicts what could be collected by a network operating on a 15-min sampling frequency to a 3-km ceiling. However, this sampling frequency and target flight ceiling poses a great operational challenge when considering battery life and UAV ascent rates. This simulation does suggest that at least a 30-min cadence is useful (Fig. 11d); however, a more thorough study of the temporal evolution of these systems is required to make an accurate recommendation. Future OSSEs and modeling studies need to take these scientific details into account while also considering the technical and logistical constraints of battery consumption, UAV ascent rates, and icing. All of these operational and scientific questions are important to bear in mind to guide future research efforts and drive advances in UAV capabilities.

5. Summary and discussion

Resolving winter-weather hydrometeor types in transition zones requires high spatial and temporal resolution. These hydrometeor types are sensitive to how much melting or refreezing occurs in the lowest few kilometers of the atmosphere. Additionally, a perturbation in the vertical profile as little as 0.5°C can alter the precipitation type and thus presents a daunting task for numerical weather models. In this study, UAVs and radiosondes are utilized to sample a mixed-phase winter environment and are compared against the HRRR 0-h analyses to assess the benefits of high-resolution observations.
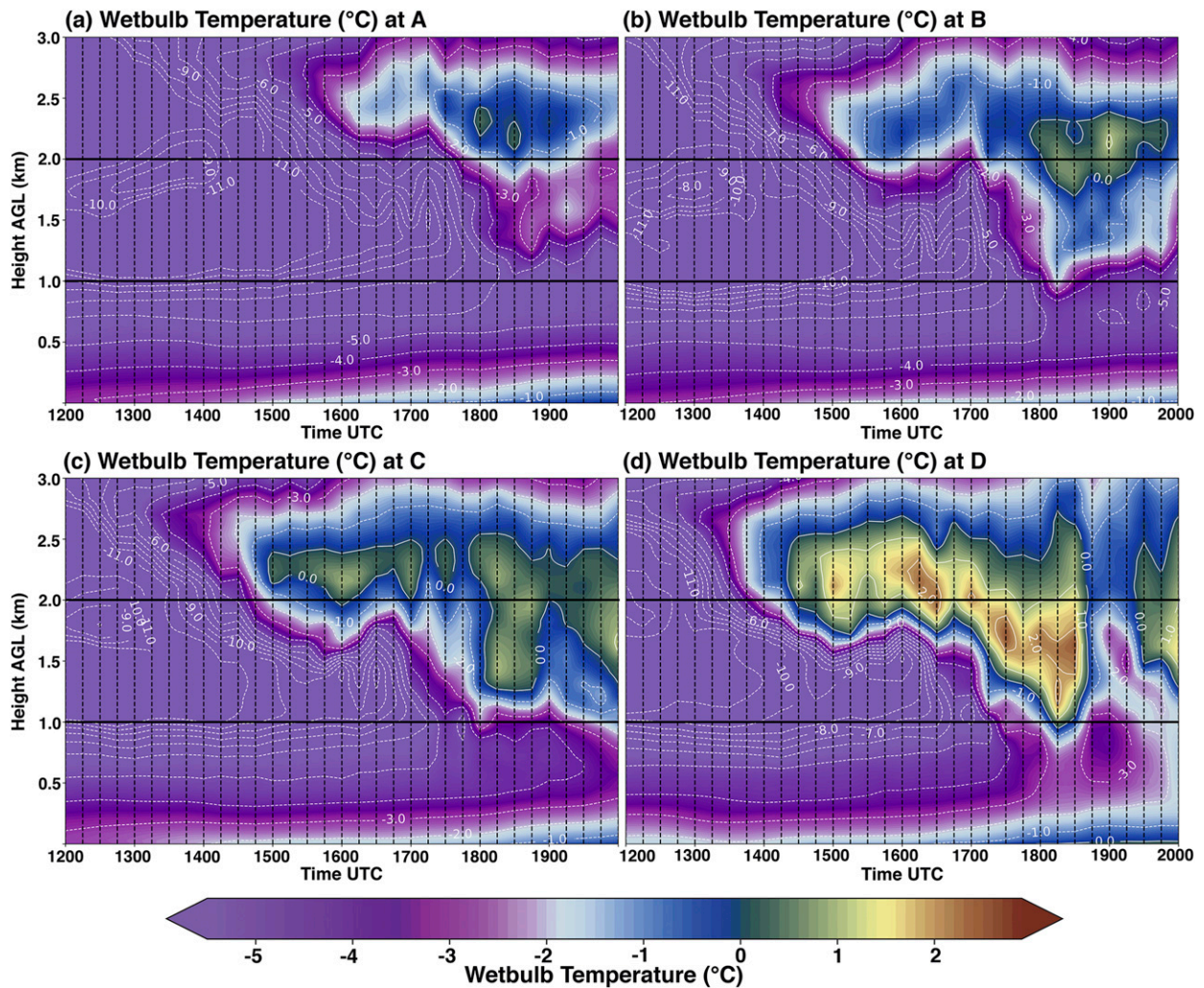
FIG. 11. Plots of time (UTC) vs height (km) of the WRF-simulated 19 Feb 2019 Oklahoma winter storm. Point locations (A, B, C, and D) are denoted in Fig. 10. Wet-bulb temperature (°C) is given at locations (a) A, (b) B, (c) C, and (d) D. Sampling frequency is denoted by the dashed vertical lines. Solid contours denote values above 0°C, and dashed contours are values below 0°C. The 1- and 2-km heights (AGL) are denoted by horizontal black lines.

UAV and radiosonde measurements agree well and identify a colder refreezing layer than the HRRR (up to 3°C), which leads to the production of ice pellets. The HRRR analysis of the event resolves the winter-weather environment well in terms of melting- and refreezing-layer thickness and placement of the surface 0°C isotherm. However, fine-scale thermodynamic processes are not captured at KAEFS (by the HRRR) that play an important role in diagnosing the surface precipitation type. Vertical profiles of observed and HRRR wet-bulb temperature are used as input to a hydrometeor-phase algorithm to evaluate whether the above differences are important for precipitation-type diagnosis. Both the radiosonde and UAV profiles result in a correct diagnosis of ice pellets while the HRRR profile results in a diagnosis of freezing rain/drizzle. Such results indicate that collecting observations using a UAV network can add value for the detection and nowcasting of mixed-phase winter-weather events.

A WRF modeling study was conducted for illustrative purposes to show hypothetical observations from a UAV network and to highlight some of the operational and scientific questions that need to be addressed in future research. When examining simulated UAV data at four mesonet locations, small variations in thermodynamic measurements captured by UAVs across a transition zone show promise in capturing valuable information that is not observed in the current radiosonde network. Future OSSEs and modeling studies are needed to understand what impact these observations could have and what network configurations have the greatest impact on operational NWP. Other factors such as flight ceilings, sampling frequency, VLOS requirements, battery life, and UAV ascent rates are among the many topics that need to be thoroughly vetted in future UAV winter-weather research efforts.

This case study represents a small sample of UAV data collected in winter-weather environments. Further investigation

including more case studies needs to be conducted to better quantify winter-weather conditions that occur in the Oklahoma Mesonet domain. The authors strongly suggest an extensive study be conducted on icing and other related meteorological conditions that could limit UAV flight performance in winter weather. There was some evidence of icing on the instrumentation utilized in this case study. Icing can cause slowed sensor response time and erroneous measurements, which contaminate observations collected in these environments. Characterization of sensors in icing conditions and in-flight deicing mitigation is critical to the success in collecting these measurements.

Moving forward toward an operational network, permissions for beyond visual line-of-sight (BVLOS) will be required to operate multiple UAVs in a mesoscale network and to capture important data above cloud base. The FAA has begun granting BVLOS permissions to industry partners and large operational teams who provide evidence of superior operational excellence with proven risk-mitigation systems. Whereas BVLOS is plausible from an operational standpoint (Chilson et al. 2019), significant testing of in-cloud measurements needs to be conducted to ensure accurate measurements can be collected. Additionally, work to create an artificial intelligence network for meteorological flight conditions is necessary for this type of an observational network.

This study focused on utilizing UAVs in environments near 0°C due to the importance of small PBL temperature changes. However, cases of extreme winter weather, such as blizzards, lake-effect snow, or snow squalls were not explored. These environments are strongly driven by synoptic and convective processes on varying spatial and temporal scales. Additionally, wind fields associated with these winter-weather types pose an extreme challenge for UAV flight performance. Future work assessing UAV operations in these types of winter weather systems is necessary moving forward.

REFERENCES

Alexander, C. R., and Coauthors, 2017: Expanding the High-Resolution Rapid Refresh (HRRR) from deterministic to ensemble data assimilation, forecasts and post-processing. *28th Conf. on Weather Analysis and Forecasting/24th Conf. on Numerical Weather Prediction*, Seattle, WA, Amer. Meteor. Soc., 3B.5, https://ams.confex.com/ams/97Annual/webprogram/Paper309424.html.

Barbieri, L., and Coauthors, 2019: Intercomparison of small unmanned aircraft system (sUAS) measurements for atmospheric science during the LAPSE-RATE campaign. *Sensors*, **19**, 2179, https://doi.org/10.3390/s19092179.

Bell, T. M., B. R. Greene, P. M. Klein, M. Carney, and P. B. Chilson, 2020: Confronting the boundary layer data gap: Evaluating new and existing methodologies of probing the lower atmosphere. *Atmos. Meas. Tech.*, **13**, 3855–3872, https://doi.org/10.5194/amt-13-3855-2020.

Benjamin, S. G., and Coauthors, 2016: A North American hourly assimilation and model forecast cycle: The Rapid Refresh. *Mon. Wea. Rev.*, **144**, 1669–1694, https://doi.org/10.1175/MWR-D-15-0242.1.

Brock, F. V., K. C. Crawford, R. L. Elliott, G. W. Cuperus, S. J. Stadler, H. L. Johnson, and M. D. Eilts, 1995: The Oklahoma Mesonet: A technical overview. *J. Atmos. Oceanic Technol.*, **12**, 5–19, https://doi.org/10.1175/1520-0426(1995)012<0005:TOMATO>2.0.CO;2.

Burg, T., K. L. Elmore, and H. M. Grams, 2017: Assessing the skill of updated precipitation-type diagnostics for the Rapid Refresh with mPING. *Wea. Forecasting*, **32**, 725–732, https://doi.org/10.1175/WAF-D-16-0132.1.

Call, D. A., 2010: Changes in ice storm impacts over time: 1886–2000. *Wea. Climate Soc.*, **2**, 23–35, https://doi.org/10.1175/2009WCAS1013.1.

Cassano, J. J., M. W. Seefeldt, S. Palo, S. L. Knuth, A. C. Bradley, P. D. Herrman, P. A. Kernebone, and N. J. Logan, 2016: Observations of the atmosphere and surface state over Terra Nova Bay, Antarctica, using unmanned aerial systems. *Earth Syst. Sci. Data*, **8**, 115–126, https://doi.org/10.5194/essd-8-115-2016.

Changnon, S. A., 2003: Characteristics of ice storms in the United States. *J. Appl. Meteor.*, **42**, 630–639, https://doi.org/10.1175/1520-0450(2003)042<0630:COISIT>2.0.CO;2.

——, and T. R. Karl, 2003: Temporal and spatial variations of freezing rain in the contiguous United States: 1948–2000. *J. Appl. Meteor.*, **42**, 1302–1315, https://doi.org/10.1175/1520-0450(2003)042<1302:TASVOF>2.0.CO;2.

——, D. Changnon, and T. R. Karl, 2006: Temporal and spatial characteristics of snowstorms in the contiguous United States. *J. Appl. Meteor. Climatol.*, **45**, 1141–1155, https://doi.org/10.1175/JAM2395.1.

Chilson, P. B., and Coauthors, 2019: Moving towards a network of autonomous UAS atmospheric profiling stations for observations in the earth's lower atmosphere: The 3D mesonet concept. *Sensors*, **19**, 2720, https://doi.org/10.3390/s19122720.

Curry, J. A., J. Maslanik, G. Holland, and J. Pinto, 2004: Applications of aerosondes in the Arctic. *Bull. Amer. Meteor. Soc.*, **85**, 1855–1862, https://doi.org/10.1175/BAMS-85-12-1855.

de Boer, G., and Coauthors, 2016: The Pilatus unmanned aircraft system for lower atmospheric research. *Atmos. Meas. Tech.*, **9**, 1845–1857, https://doi.org/10.5194/amt-9-1845-2016.

——, and Coauthors, 2018: A bird's-eye view: Development of an operational ARM unmanned aerial capability for atmospheric research in Arctic Alaska. *Bull. Amer. Meteor. Soc.*, **99**, 1197–1212, https://doi.org/10.1175/BAMS-D-17-0156.1.

——, and Coauthors, 2020: Development of community, capabilities, and understanding through unmanned aircraft-based atmospheric research: The LAPSE-RATE campaign. *Bull. Amer. Meteor. Soc.*, **101**, E684–E699, https://doi.org/10.1175/BAMS-D-19-0050.1.

Elmore, K. L., Z. L. Flamig, V. Lakshmanan, B. T. Kaney, V. Farmer, H. D. Reeves, and L. P. Rothfusz, 2014: MPING: Crowd-sourcing weather reports for research. *Bull. Amer. Meteor. Soc.*, **95**, 1335–1342, https://doi.org/10.1175/BAMS-D-13-00014.1.

——, H. M. Grams, D. Apps, and H. D. Reeves, 2015: Verifying forecast precipitation type with mPING. *Wea. Forecasting*, **30**, 656–667, https://doi.org/10.1175/WAF-D-14-00068.1.

Elston, J. S., J. Roadman, M. Stachura, B. Argrow, A. Houston, and E. Frew, 2011: The tempest unmanned aircraft system for in situ observations of tornadic supercells: Design and VORTEX2 flight results. *J. Field Robot.*, **28**, 461–483, https://doi.org/10.1002/rob.20394.

Greene, B. R., A. R. Segales, S. Waugh, S. Duthoit, and P. B. Chilson, 2018: Considerations for temperature sensor placement on rotary-wing unmanned aircraft systems. *Atmos. Meas. Tech.*, **11**, 5519–5530, https://doi.org/10.5194/amt-11-5519-2018.

——, ——, T. M. Bell, E. A. Pillar-Little, and P. B. Chilson, 2019: Environmental and sensor integration influences on temperature measurements by rotary-wing unmanned aircraft systems. *Sensors*, **19**, 1470, https://doi.org/10.3390/s19061470.

Grout, T., Y. Hong, J. Basara, B. Balasundaram, Z. Kong, and S. T. S. Bukkapatnam, 2012: Significant winter weather events and associated socioeconomic impacts (federal aid expenditures) across Oklahoma: 2000–10. *Wea. Climate Soc.*, **4**, 48–58, https://doi.org/10.1175/WCAS-D-11-00057.1.

Houston, A. L., B. Argrow, J. Elston, J. Lahowetz, E. W. Frew, and P. C. Kennedy, 2012: The collaborative Colorado–Nebraska unmanned aircraft system experiment. *Bull. Amer. Meteor. Soc.*, **93**, 39–54, https://doi.org/10.1175/2011BAMS3073.1.

Iacono, M. J., J. S. Delamere, E. J. Mlawer, M. W. Shephard, S. A. Clough, and W. D. Collins, 2008: Radiative forcing by long-lived greenhouse gases: Calculations with the AER radiative transfer models. *J. Geophys. Res.*, **113**, D13103, https://doi.org/10.1029/2008JD009944.

Ikeda, K., M. Steiner, and G. Thompson, 2017: Examination of mixed-phase precipitation forecasts from the high-resolution rapid refresh model using surface observations and sounding data. *Wea. Forecasting*, **32**, 949–967, https://doi.org/10.1175/WAF-D-16-0171.1.

Inoue, J., J. A. Curry, and J. A. Maslanik, 2008: Application of aerosondes to melt-pond observations over Arctic sea ice. *J. Atmos. Oceanic Technol.*, **25**, 327–334, https://doi.org/10.1175/2007JTECHA955.1.

Jacob, J. D., P. B. Chilson, A. L. Houston, and S. W. Smith, 2018: Considerations for atmospheric measurements with small unmanned aircraft systems. *Atmosphere*, **9**, 252, https://doi.org/10.3390/atmos9070252.

Koch, S. E., M. Fengler, P. B. Chilson, K. L. Elmore, B. Argrow, D. L. Andra, and T. Lindley, 2018: On the use of unmanned aircraft for sampling mesoscale phenomena in the preconvective boundary layer. *J. Atmos. Oceanic Technol.*, **35**, 2265–2288, https://doi.org/10.1175/JTECH-D-18-0101.1.

McCray, C. D., E. H. Atallah, and J. R. Gyakum, 2019: Long-duration freezing rain events over North America: Regional climatology and thermodynamic evolution. *Wea. Forecasting*, **34**, 665–681, https://doi.org/10.1175/WAF-D-18-0154.1.

McPherson, R. A., and Coauthors, 2007: Statewide monitoring of the mesoscale environment: A technical update on the Oklahoma Mesonet. *J. Atmos. Oceanic Technol.*, **24**, 301–321, https://doi.org/10.1175/JTECH1976.1.

Moore, A., 2018: Observing system simulation experiment studies on the use of small UAV for boundary-layer sampling. M.S. thesis, University of Oklahoma, 147 pp.

Nakanishi, M., and H. Niino, 2006: An improved Mellor–Yamada level-3 model: Its numerical stability and application to a regional prediction of advection fog. *Bound.-Layer Meteor.*, **119**, 397–407, https://doi.org/10.1007/s10546-005-9030-8.

National Weather Service, 1998: Automated Surface Observing System (ASOS) user's guide. NOAA/NWS Doc., 59 pp., https://www.weather.gov/media/asos/aum-toc.pdf.

NRC, 2009: *Observing Weather and Climate from the Ground Up: A Nationwide Network of Networks*. National Academies Press, 250 pp., https://doi.org/10.17226/12540.

Pillar-Little, E. A., and Coauthors, 2021: Observations of the thermodynamic and kinematic state of the atmospheric boundary layer over the San Luis Valley, CO, using the CopterSonde 2 remotely piloted aircraft system in support of the LAPSE-RATE field campaign. *Earth Syst. Sci. Data*, **13**, 269–280, https://doi.org/10.5194/essd-13-269-2021.

Ralph, F., and Coauthors, 2005: Improving short-term (0 48 h) cool-season quantitative precipitation forecasting: Recommendations from a USWRP workshop. *Bull. Amer. Meteor. Soc.*, **86**, 1619–1632, https://doi.org/10.1175/BAMS-86-11-1619.

Rauber, R. M., L. S. Olthoff, M. K. Ramamurthy, D. Miller, and K. E. Kunkel, 2001: A synoptic weather pattern and sounding-based climatology of freezing precipitation in the United States east of the Rocky Mountains. *J. Appl. Meteor.*, **40**, 1724–1747, https://doi.org/10.1175/1520-0450(2001)040<1724:ASWPAS>2.0.CO;2.

Reeves, H. D., 2016: The uncertainty of precipitation-type observations and its effect on the validation of forecast precipitation type. *Wea. Forecasting*, **31**, 1961–1971, https://doi.org/10.1175/WAF-D-16-0068.1.

——, and J. Waters, 2019: Dual-polarized radar coverage in terminal airspaces and its effect on interpretation of winter weather signatures: Current capabilities and future recommendations. *J. Appl. Meteor. Climatol.*, **58**, 165–183, https://doi.org/10.1175/JAMC-D-18-0123.1.

——, K. L. Elmore, A. Ryzhkov, T. Schuur, and J. Krause, 2014: Sources of uncertainty in precipitation-type forecasting. *Wea. Forecasting*, **29**, 936–953, https://doi.org/10.1175/WAF-D-14-00007.1.

——, A. V. Ryzhkov, and J. Krause, 2016: Discrimination between winter precipitation types based on spectral-bin microphysical modeling. *J. Appl. Meteor. Climatol.*, **55**, 1747–1761, https://doi.org/10.1175/JAMC-D-16-0044.1.

Reuder, J., P. Brisset, M. Jonassen, M. Müller, and S. Mayer, 2008: SUMO: A small unmanned meteorological observer for atmospheric boundary layer research. *IOP Conf. Ser. Earth Environ. Sci.*, **1**, 012014, https://doi.org/10.1088/1755-1315/1/1/012014.

Segales, A. R., B. Greene, T. Bell, W. Doyle, J. Martin, E. Pillar-Little, and P. Chilson, 2020: The CopterSonde: An insight into the development of a smart UAS for atmospheric boundary layer research. *Atmos. Meas. Tech,* **13**, 2833–2848, https://doi.org/10.5194/amt-13-2833-2020.

Skamarock, W. C., and Coauthors, 2019: A description of the Advanced Research WRF model version 4. NCAR Tech. Note NCAR/TN-556+STR, 162 pp., https://doi.org/10.5065/1dfh-6p97.

Smirnova, T. G., J. M. Brown, S. G. Benjamin, and J. S. Kenyon, 2016: Modifications to the Rapid Update Cycle Land Surface Model (RUC LSM) available in the Weather Research and Forecasting (WRF) Model. *Mon. Wea. Rev.*, **144**, 1851–1865, https://doi.org/10.1175/MWR-D-15-0198.1.

Stewart, R. E., J. M. Thériault, and W. Henson, 2015: On the characteristics of and processes producing winter precipitation types near 0°. *Bull. Amer. Meteor. Soc.*, **96**, 623–639, https://doi.org/10.1175/BAMS-D-14-00032.1.

Thériault, J. M., R. E. Stewart, and W. Henson, 2010: On the dependence of winter precipitation types on temperature, precipitation rate, and associated features. *J. Appl. Meteor. Climatol.*, **49**, 1429–1442, https://doi.org/10.1175/2010JAMC2321.1.

Thompson, E. J., S. A. Rutledge, B. Dolan, V. Chandrasekar, and B. L. Cheong, 2014: A dual-polarization radar hydrometeor classification algorithm for winter precipitation. *J. Atmos. Oceanic Technol.*, **31**, 1457–1481, https://doi.org/10.1175/JTECH-D-13-00119.1.

Thompson, G., P. R. Field, R. M. Rasmussen, and W. D. Hall, 2008: Explicit forecasts of winter precipitation using an improved bulk microphysics scheme. Part II: Implementation of a new snow parameterization. *Mon.*

Wea. Rev., **136**, 5095–5115, https://doi.org/10.1175/2008MWR2387.1.

Waugh, S., and T. J. Schuur, 2018: On the use of radiosondes in freezing precipitation. *J. Atmos. Oceanic Technol.*, **35**, 459–472, https://doi.org/10.1175/JTECH-D-17-0074.1.

Zhang, J., and Coauthors, 2016: Multi-Radar Multi-Sensor (MRMS) quantitative precipitation estimation: Initial operating capabilities. *Bull. Amer. Meteor. Soc.*, **97**, 621–638, https://doi.org/10.1175/BAMS-D-14-00174.1.